Composites Part B 247 (2022) 110297

Contents lists available at ScienceDirect

Composites Part B

journal homepage: www.elsevier.com/locate/compositesb

Preferred orientation of calcium silicate hydrate and its implication to concrete creep

Jiaqi Li [a,*], Wenxin Zhang [b]

[a] Atmospheric, Earth, and Energy Division, Lawrence Livermore National Laboratory, CA, United States
[b] Department of Mechanical and Civil Engineering, California Institute of Technology, United States

ARTICLE INFO

Keywords:
C-S-H
Texture formation
High pressure X-ray diffraction
Deviatoric stress
Mechanics

ABSTRACT

Calcium silicate hydrate (C–S–H) is the primary binding phase of cement-based and alkali-activated materials. The preferred orientation of C–S–H under non-hydrostatic pressure (e.g., uniaxial/biaxial load) is overlooked yet crucial in understanding concrete's multiscale mechanical performance. Here, we unveil the texture formation of C–S–H under compressive deviatoric stress, S, from 0 to ~200 MPa, using high-pressure X-ray diffraction. Texture initiated at S < 12 MPa: the *c*-axis (normal to the basal plane) of C–S–H nanocrystallites preferentially re-oriented towards the direction of the principal compressive stress. Below S ~100 MPa, the preferred orientation intensified through translation and rotation of C–S–H nanocrystallites; above ~100 MPa, the texture stopped growing then weakened, suggesting internal transformations of C–S–H nanocrystallites. The time-dependence of the preferred orientation development is unveiled by the texture weakening after full unloading. The findings implicate that concrete creep under service loads is contributed by the intergranular preferential re-orientation of C–S–H nanocrystallites, not interlayer sliding or silicate chain breakage.

1. Introduction

Cement-based materials (e.g., concrete) are widely used in energy and civil infrastructure systems, e.g., buildings, power plants, and oil well cementing [1]. Understanding the mechanical properties and behaviors (e.g., creep) of cement-based materials is critical to designing adaptive, resilient, and robust infrastructure [2]. The mechanical properties and creep of cement-based materials are governed by their primary binding phase, calcium silicate hydrate (C–S–H) [1]. However, understanding the mechanical properties and creep of C–S–H is challenging due to the complex nature of C–S–H [3]. C–S–H is highly porous at mesoscale with coherent domain sizes of 3–5 nm [4] and often intermixes with portlandite [5]. C–S–H has variable chemical compositions with Ca/Si molar ratios of 1.2–2.3 and an average of ~1.75 in hardened ordinary Portland cement [6]. C–S–H is X-ray amorphous at ambient temperature, thus understanding its crystal structure is challenging [7].

Phase-pure nanocrystalline C–S–H (also termed C–S–H I) can be synthesized to address the challenges in the studies of complex C–S–H in cement pastes [8]. The nanostructure of C–S–H I is similar to a defected tobermorite [9]: "dreierketten" silicate chains (one bridging tetrahedra site connects two paired sites repeatedly) are flanked on CaO_7 sheet with water and Ca filled in the interlayer. As the Ca/Si ratio increases, the bridging silicate is replaced with Ca, leading to shorter mean silicate chains [10]. Due to its phase-pure and nanocrystalline nature, the structure and mechanical properties of C–S–H I have been extensively studied [11,12].

Existing mechanical models (e.g., elastic properties and creep) of cement-based materials [13,14] assume uniformly or randomly distributed representative volume elements, and the assumed material properties are isotropic at meso- and macro-scale. The orientation distribution of domains of hydration/activation products (e.g., C–S–H, portlandite, and ettringite) in existing models is random or omitted [15,16]. However, a recent study has shown that the preferred orientation distribution (also known as texture) of cross-linked calcium aluminosilicate hydrate (C-A-S-H, an Al-tobermorite-like phase with a nanostructure similar to C–S–H) nanocrystallites, ettringite, and portlandite crystals occurs under deviatoric stress [17]. This term "texture" only refers to the orientation distribution of polycrystalline materials, not the microstructure of cement phases. The layered C-A-S-H nanocrystallites prefer to align with their *c*-axis (normal to the basal plane) parallel to the principal compression direction. For cross-linked C-A-S-H

* Corresponding author.Lawrence Livermore National Laboratory, 7000 East Avenue, Livermore, CA, 94550, United States.
E-mail address: li88@llnl.gov (J. Li).

https://doi.org/10.1016/j.compositesb.2022.110297
Received 17 February 2022; Received in revised form 28 August 2022; Accepted 14 September 2022
Available online 20 September 2022

nanocrystallites, this texture formed at above ~0.4 GPa of uniaxial compression. The texture formation of these polycrystalline materials may lead to anisotropic properties at the macroscale [18]. Although ~0.4 GPa of uniaxial compressive stress is much higher than the compressive strength of concrete [19,20], the results in our previous study still indicate that the orientation of cement phases (e.g., ettringite) may not be randomly distributed in concrete's service life and the macro properties of concrete may not be isotropic [21]. The existing concrete models of mechanical performance may not truly represent the concrete structure and properties under service loads. Therefore, studies of the deviatoric stress-induced preferred orientation of non-cross-linked C–S–H (i.e., C–S–H in cement pastes) are necessary. Validating the preferred orientation of C–S–H can improve the understanding of the properties, structure, and chemistry of C–S–H in fields where concrete structures often sustain compressive loads.

Creep is important for the structural integrity of cement-based materials under long-term service [22]. Although it has been generally agreed that cement creep is associated with the viscoelastic nature of C–S–H, relative humidity (RH), and stress level [23–25], the creep mechanism of C–S–H remains hotly debated. Different theories of creep have been proposed: microprestress-induced shear slips between walls of the micropores [26]; stress-induced sliding at the interlayer of C–S–H [27]; stress-induced dissolution-reprecipitation of C–S–H [28]; stress-induced reorganization of C–S–H nanoglobules [13]. Nevertheless, there is a lack of experimental evidence of the creep theories at the nanoscale. Our recent study has correlated the time-dependent and RH-dependent preferred orientation of cross-linked C-A-S-H with the origin of the creep of cement. However, the exact deviatoric stress levels in our previous study are unknown. The preferred orientation of non-cross-linked C–S–H nanograins under much lower stress has not been studied, which can be more direct evidence of the reorganization of C–S–H particles as the origin of cement creep. The study of the preferred orientation of non-cross-linked C–S–H can eliminate the effects of cross-linking aluminate/silicate sites of C-A-S-H on the studies of mechanical behaviors of layered nanocrystallites.

In this study, C–S–H I under deviatoric stress is studied using in-situ high-pressure X-ray diffraction to elaborate the texture development and creep of C–S–H. The nanocrystalline C–S–H I sample is dimer-only (pairs of silicate tetrahedra bound via common oxygen to two Ca atoms from the Ca–O layer, see Fig. 1), as C–S–H at high Ca/Si ratios (here, 1.47) often shows intense basal plane diffraction [11]. Deviatoric stress is provided as no pressure-transmitting medium is used in a diamond anvil cell (DAC). Deviatoric stress as low as ~12 MPa is applied. The time-dependence of the preferred orientation of C–S–H nanocrystallites was confirmed through stress recovery. The findings in this study provide implications to advance the understanding of the creep of cement-based materials and are critical for improving the mechanical modeling of cement-based materials. Since C–S–H I is also the primary phase of alkali-activated materials [29,30], the present study also provides implications for designing sustainable and robust alkali-activated materials. The findings are also relevant to the modeling of C–S–H I-rich cement systems (e.g., blended cement and degraded cement by decalcification [31]).

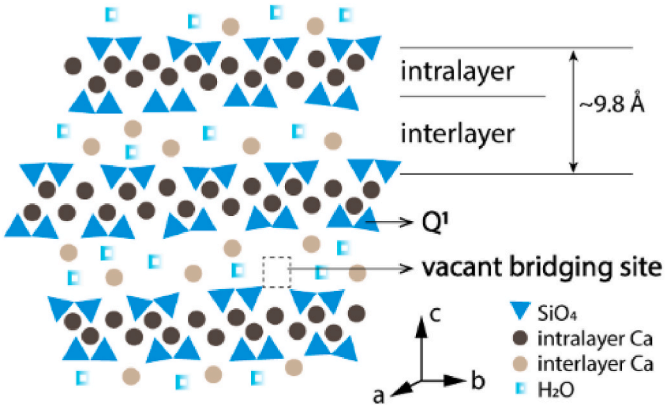

Fig. 1. Schematic representation of the nanostructure of C–S–H at bulk Ca/Si of 1.47 used in this study. It predominantly comprises of Q^1 silicates, in the absence of bridging or cross-linking silicates, with a mean silicate chain length of two.

2. Materials and method

2.1. Materials

Stoichiometric amounts of CaO and fumed SiO_2 (Aerosil 200, Evonik) were mixed with deionized water at an initial bulk Ca/Si molar ratio of 1.6 and a water-to-solid mass ratio of 45. The slurry was cured at 20 °C for one year under N_2 protection. The one-year curing ensures all initial $Ca(OH)_2$ is consumed to react with SiO_2. The final slurry was vacuum-filtered and freeze-dried for seven days in a N_2-filled environment. More details can be found elsewhere [32]. The final bulk Ca/Si ratio of the C–S–H is 1.47. The dried sample is $Ca(OH)_2$-free because the initial Ca is partially dissolved in the high volume of deionized water [32].

2.2. HP-XRD in radical diffraction geometry

The HP-XRD measurement was performed at the superbend beamline 12.2.2 of the Advanced Light Source at the Lawrence Berkeley National Laboratory. The beam has a wavelength of 0.4979 Å and a spot size of ~30 μm. A radial geometry BX90 diamond anvil cell (DAC) was used [33]. This radial geometry DAC has a wider opening for diffracted beams compared to axial geometry BX90 used in our previous studies [34,35]. This geometry allowed us to probe the crystal orientations relative to the compression direction (Fig. 2). A 65 μm thick boron epoxy resin gasket inserted into a hole of a polyimide film (~100 μm thick) was used. A stainless-steel gasket was not used as it would absorb most of the beam in the radial geometry. A chamber with a diameter of 120 μm was drilled at the center of the boron epoxy resin gasket by laser milling.

A diffraction pattern at ambient pressure was taken from C–S–H powder mounted in a glass capillary. For the HP-XRD experiment, the C–S–H powder sample was lightly packed into the gasket chamber with ~2/3 of the volume. A few mg of platinum powder was lightly packed into a thin Pt plate and placed between the sample and one diamond anvil culet (~400 μm diameter). No pressure-transmitting medium was used in this study so that by tightening the loading screws of the DAC, deviatoric stresses developed in the sample chamber. The initial stress in the chamber was zero. Tightening the screws applies compression on the

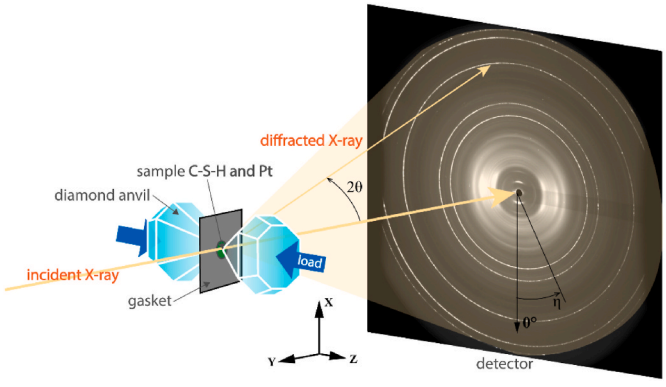

Fig. 2. Schematic representation of the DAC radial diffraction geometry. The Y-axis is aligned with the incident beam path, and the *Z*-axis is aligned with the axis of DAC.

sample chamber along *Z*-axis through the flat ends of the diamond anvils of the DAC, while the chamber is confined by the boron epoxy gasket on the face normal to the *Z*-axis (Fig. 2). After the inter-grain pores were eliminated by increasing compression, the stress began to increase. At each pressure point, the diffraction of Pt was analyzed to compute the deviatoric stress and hydrostatic pressure in the chamber. An equivalent stress state of C-S-H nanocrystallites and the Pt grains is assumed. This Reuss approximation is often accepted in DACs with radial geometry in geophysics studies [36]. The applied hydrostatic pressure, P, of Pt was determined from the volumetric change of a Pt unit cell using Vinet equation of state [37]. The pressure-dependent stiffness tensor of Pt was used to refine deviatoric stress, S, using the BulkPathGEO method and the Moment pole stress model imbedded in MAUD (Materials Analysis Using Diffraction, a Rietveld extended program to perform the diffraction analysis) [38]. The non-zero components of the macroscopic elastic stress tensor in this geometry can be expressed as $\sigma_{xx} = \sigma_{yy} = P–S$ and $\sigma_{zz} = P + 2S$, where compression is represented with the positive sign.

A diffraction image at each pressure point was recorded by a MAR345 area detector with an exposure time of 600 s. The compression was sustained for ~30 min at each pressure point. 14 data points were collected along the loading path, another 11 data points were collected along the unloading path back to ambient condition, and one data point was collected 6 h after full unloading for the identification of stress recovery. The 6-h recovery was the longest time that we can wait as the beamtime of synchrotron-radiation-based HP-XRD is very precious. Commercially-available laboratory-based diffractometers cannot provide the beam brightness and geometry for our experimental setup. At each loading/unloading step, the hydrostatic pressure P and the deviatoric stress S were refined from the Pt diffraction pattern (Fig. 3). The slightly negative (i.e., tensile) deviatoric stress refined from the first loading step is explained by the initial abnormal stress development before the true compaction to the power sample in the chamber. At maximum, P ~4.9 GPa and S ~0.2 GPa were achieved. Negligible residual P existed after full unloading, but the residual S was −14 MPa. The 6-hr recovery led to the relaxation of the S from −14 MPa to 1 MPa. As mentioned earlier, a boron epoxy gasket must be used to sustain the pressure from the diamond anvils in the radial geometry in this study. Boron epoxy is fragile and typically starts to crack with inelastic deformations during loading at the hydrostatic pressure level of 100s MPa. Thus, gradual unloading of a cracked boron epoxy gasket from ~5 GPa to 0 with a similar/constant pressure step size is challenging. A sudden drop of hydrostatic pressure P from 3044 MPa to 113 MPa does not affect the findings and conclusions in the present study.

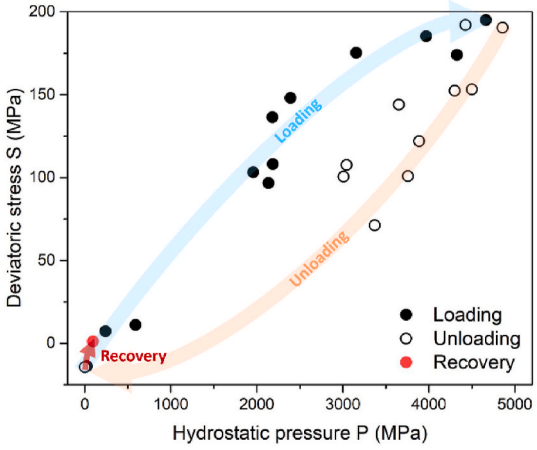

Fig. 3. The relationship between the hydrostatic pressure P and the deviatoric stress S refined with the Pt diffractions. The loading, unloading, and recovery path are indicated with blue, orange, and red arrows, respectively, for eye guidance. (For interpretation of the references to colour in this figure legend, the reader is referred to the Web version of this article.)

The diffraction pattern at each pressure point was refined with monoclinic B11m tobermorite using the MAUD package [39]. As shown in Fig. 4, the diffraction of the boron epoxy gasket overlaps with most of the peaks of C–S–H except the (002) basal peak. The (002) peak is the most representative for texture analysis of C–S–H; thus, only the lattice parameter c was refined using MAUD in the present study. At each pressure point, the right half of each raw diffraction image was not used for refinement as the (002) Debye ring here was affected by artifacts (i.e., background noise from the gasket and beam-stop). The left half of each image was sliced into 36 sectors at every 5° in the azimuthal angle. Each sector was integrated into a 1D diffraction pattern as a refinement input.

The orientation distribution function (ODF) of C–S–H nanocrystals in this study was refined using the standard fiber model function. The ODF is analogous to the probability distribution function for random variables and for spatial directions. In the present study, the (002) texture suggests the use of the standard function imposing a fiber component along the crystal *c*-axis to the center of the pole figure (while nonzero ThetaY indicates the degree of misalignment between the crystal *c*-axis and the global *Z*-axis). Max and Min values are in the unit of multiples of random distribution, with higher Max values and lower Min values indicating greater deviation from a uniform random distribution and thus greater texturing. FWHM may be qualitatively understood as the variation of the crystal *c*-axis orientations – thus, a smaller FWHM suggests a stronger texture. Note that the fiber term here only refers to the crystal orientation rather than the morphology of hydrate grains in cement chemistry. The possible tilt between the fiber axis and the *Z*-axis in the sample coordination due to the misalignment of diamond culets was also refined.

3. Results and discussion

Fig. 5 compares the raw 2D images of the present sample and that of the same C–S–H sample under pure hydrostatic pressure. Azimuthal angle-dependent diffraction intensity of the C–S–H planes ((002), (200), and ($\bar{2}$ 20) (020)) was observed in the present sample (left half) under deviator stress S = 0.1 GPa, but absent in the purely hydrostatically loaded reference (right half) with deviator stress S = 0 GPa. For

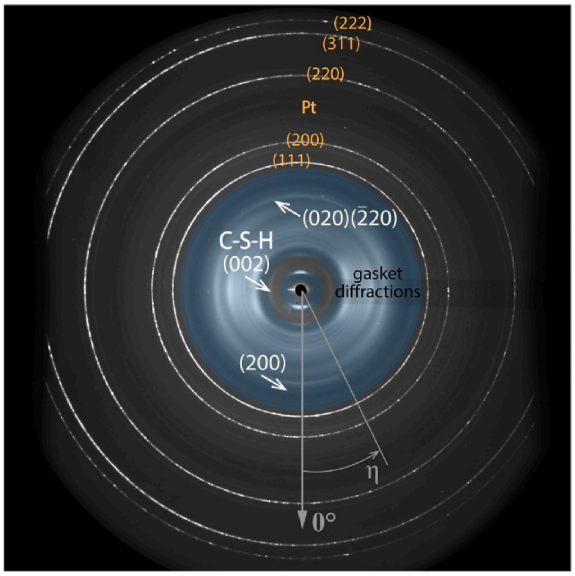

Fig. 4. Raw 2D diffraction image of the sample. The diffraction from C–S–H (002) plane is labeled in white, the diffractions from Pt are labeled in yellow, and the gasket diffractions are shaded. The 0° azimuthal angle and its direction are indicated in grey. (For interpretation of the references to colour in this figure legend, the reader is referred to the Web version of this article.)

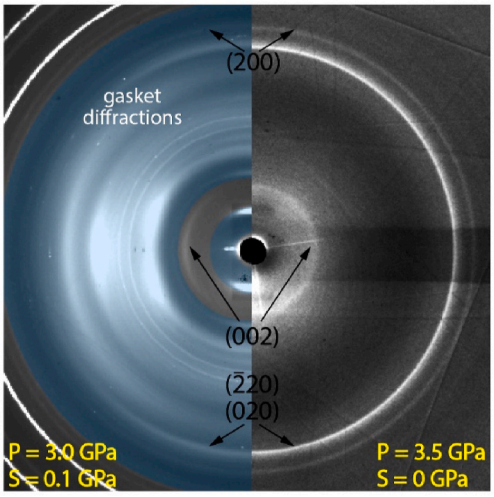

Fig. 5. The raw 2D diffraction image of the C–S–H sample with deviatoric (left) demonstrating strong variation in diffraction intensity across the azimuthal angles and without deviatoric stress (right) displaying uniform diffraction intensity. The diffractions from C–S–H are labeled in black, and the gasket diffractions are shaded.

example, the diffraction intensity of (002) plane of C–S–H under sole hydrostatic pressure is almost identical along the 0°–180° of azimuthal angle on the right, while the diffraction intensity of (002) plane of C–S–H under S = 0.1 GPa is relatively sharp at 270° but nearly invisible at ~180° and 360°. This fact confirms that the C–S–H nanocrystallites are randomly orientated under sole hydrostatic pressure but become considerably preferentially orientated with the deviatoric stress.

The 2D diffraction pattern (Fig. 6A, bottom) demonstrates the variation in the diffraction intensity over each 5° segment. The conventional diffraction pattern (Fig. 6A, top) was obtained from integration over the full range of the azimuthal angle. Most of the C–S–H diffraction peaks overlap with the gasket diffraction. Although overlapped C–S–H peaks could be subtracted from the gasket diffraction as evidenced in Ref. [17], the C–S–H diffraction planes (200) and ($\bar{2}$ 20) (020)) are out of our interest because (002) planes of C–S–H directly represent the orientation of C–S–H nanocrystallites. The boron epoxy gasket is also out of our interest. The overlap between the (002) peak and the gasket is weak. The diffraction from C–S–H (002) could be cleanly isolated (see the 2D pattern in Fig. 6A), fitted, and utilized for texture quantification.

The extent of the C–S–H preferred orientation changes considerably throughout the loading cycle (Table 1). The misalignment between *Z*-axis and the fiber direction in the texture model is characterized by ThetaY. The refined value of ThetaY is nearly zero, agreeing with the geometry that the deviatoric stress is expected to be applied along the *Z*-axis. ThetaY only deviated from zero by the end of unloading and after recovery because the C–S–H nanocrystallites were compacted with the permanent removal of some inter-grain pores after experiencing higher stress levels. After unloading of the high stress, the difference in volumetric changes (recovery) of the C–S–H compact and gasket chamber

Table 1
The stress state refined from Pt diffraction (hydrostatic pressure P and deviatoric stress S), the C–S–H unit cell parameter c, and preferred orientation of C–S–H (002) plane (FWHM of the orientation distribution function, m.r.d. range of the pole figure, and ThetaY) refined from C–S–H (002) diffraction. In the Rietveld analysis, the refinement error in S is 0.4–0.6 MPa, the error in c is < 0.2 Å, and the error in FWHM is < 2°.

P (MPa)	S (MPa)	*c* (Å)	FWHM	Max. (m.r.d.)	Min. (m.r.d.)	ThetaY
Loading						
24	−13.7	19.78	90°	2.39	0.46	5°
242	7.3	19.42	86°	2.61	0.39	−5°
590	11.1	19.32	87°	2.58	0.40	−6°
1958	103.2	18.82	82°	2.83	0.34	−4°
2135	96.7	18.82	78°	3.12	0.28	1°
2187	108.1	18.79	78°	3.14	0.28	1°
2183	136.4	18.72	83°	2.82	0.34	−9°
2391	148.0	18.65	79°	3.03	0.30	−8°
3155	175.3	18.44	78°	3.10	0.29	−7°
3969	185.2	18.19	81°	2.95	0.31	−6°
4325	174.0	18.18	82°	2.87	0.33	−6°
4425	192.0	18.08	85°	2.67	0.38	−6°
4662	195.0	18.04	87°	2.55	0.41	−7°
4857	190.4	17.97	89°	2.45	0.44	−9°
Unloading						
4500	153.2	17.93	71°	3.74	0.18	−5°
4300	152.4	18.24	74°	3.47	0.22	−6°
3886	121.9	18.22	73°	3.50	0.21	−6°
3757	100.8	18.22	72°	3.67	0.19	−6°
3652	144.0	18.34	73°	3.51	0.21	−4°
3369	71.3	18.35	73°	3.56	0.20	−4°
3008	100.5	18.40	73°	3.57	0.20	−5°
3044	107.5	18.46	69°	3.90	0.16	−9°
113	−63.1	19.43	81°	2.93	0.32	−18°
0	−14.3	19.53	86°	2.60	0.40	−22°
Recovery						
96	1.1	19.44	90°	2.42	0.44	19°

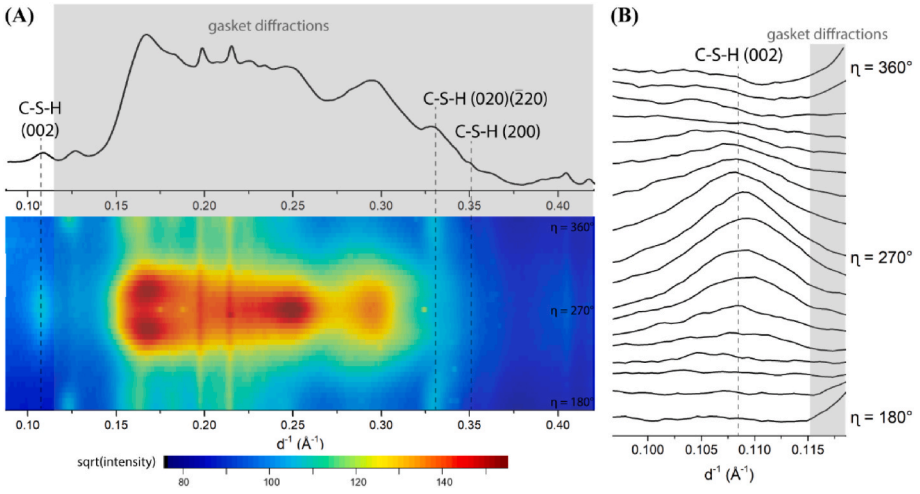

Fig. 6. Texture quantification of the sample at P = 3.0 GPa and S = 0.1 GPa: (A) the conventional diffraction pattern (top) and 2D pattern showing intensity over each 5° (bottom); (B) the diffraction patterns from C–S–H (002) stacked as a function of the azimuthal angle.

(due to the different mechanical properties of C–S–H and boron epoxy resin gasket) results in limited confinement of the recovered chamber to the compacted C–S–H, thus the tilt of the fiber axis. Such tilt is also found in a HP-XRD study of cross-linked C-A-S-H during unloading [17].

Full-width-half-maximum (FWHM) of the orientation distribution function and the maximum and minimum of the C–S–H (002) pole figure (in the unit of multiples of random distribution, m.r.d.) both express the texture intensity of C–S–H nanocrystallites. Smaller FWHM, higher maximum m.r.d., and lower minimum m.r.d. correlate to stronger texture formation. The trends in the three parameters with the stress states are equivalent (see Table 1); thus, only the evolution of FWHM is plotted against P (Fig. 7A) or S (Fig. 7B) to quantify the texture development over the loading cycle. In addition, the pole figures of C–S–H (002) planes at critical loading steps (a-c), unloading steps (d and e), and the recovery step (f) are presented below, each displaying the probability distribution of the C–S–H (002) planes, in the unit of m.r.d. In general, as seen from either the FWHM evolution (Fig. 7A and B) or the selected pole figures (Fig. 7a–f), the intensity of the C–S–H preferred orientation did not possess a linear or monotonic relationship with the applied stress level.

In our previous study of the preferred orientation of cross-linked C-A-S-H nanocrystallites [17], a strong texture (FWHM ~65° and maximum m.r.d. ~4.4) formed at the first loading step of S ~0.1 GPa, which already exceeds the stress level in ordinary concrete structures under service. In the present study, at finer loading steps, we confirmed that the texture of non-cross-linked C–S–H could form at lower deviatoric stresses with the refinement uncertainty of S at the level of 0.4–0.6 MPa (suggested in MAUD). A notable texture was observed at the first loading step (Fig. 7a). Thus, low deviatoric stress at < ~12 MPa is ample for developing a very recognizable preferred orientation of C–S–H nanocrystallites.

Albeit the varying intensity, the preferred orientation direction was consistent throughout the experiment. The maximum m.r.d. in the C–S–H (002) pole figure (Fig. 7a–f) coincided with the DAC axis, i.e., the direction of the applied deviatoric stress. This fact suggests that the *c*-axis of the C–S–H nanocrystallites tended to align with the compressive deviatoric stress. The preferred orientation gradually intensified as the sample stress reached up to P ~2 GPa and S ~0.1 GPa (step a to step b): FWHM decreased from ~90° to ~80° (Fig. 7a and b), the maximum m.r.d. increased from ~2.5 (Fig. 7a) to ~3.0 (Fig. 7b), and the minimum m.r.d. decreased from ~0.45 (Fig. 7a) to ~0.3 (Fig. 7b). As the loading continued, the strength of the C–S–H preferred orientation first plateaued until P ~4 GPa and S ~0.18 GPa, as seen from the FWHM fluctuating around ~80°. Upon further loading to the maximum values of P ~4.9 GPa and S ~0.2 GPa (step c), the texture gradually weakened but remained comparable to after the first loading step (just slightly lower FWHM, slightly greater Max, and slightly smaller Min at step c compared to step a). Accordingly, the maximum and minimum m.r.d. in Fig. 7c are between those in Fig. 7a and b.

Through unloading from maximum stresses to P ~3 GPa and S ~0.1 GPa (step c to step d), the C–S–H texture first intensified such that it became stronger than any of those refined from the loading steps and then plateaued with FWHM stabilized at ~72° (compared to ~80° during loading). The maximum m.r.d. of 3.74 in Fig. 7d exceeded the maximum m.r.d. of ~3.0 in Fig. 7b. Further unloading to the ambient condition (step d to step e) weakened texture. Immediately after complete unloading, the residual texture was stronger than that refined from the first loading step (FWHM 86° compared to 90°), despite their

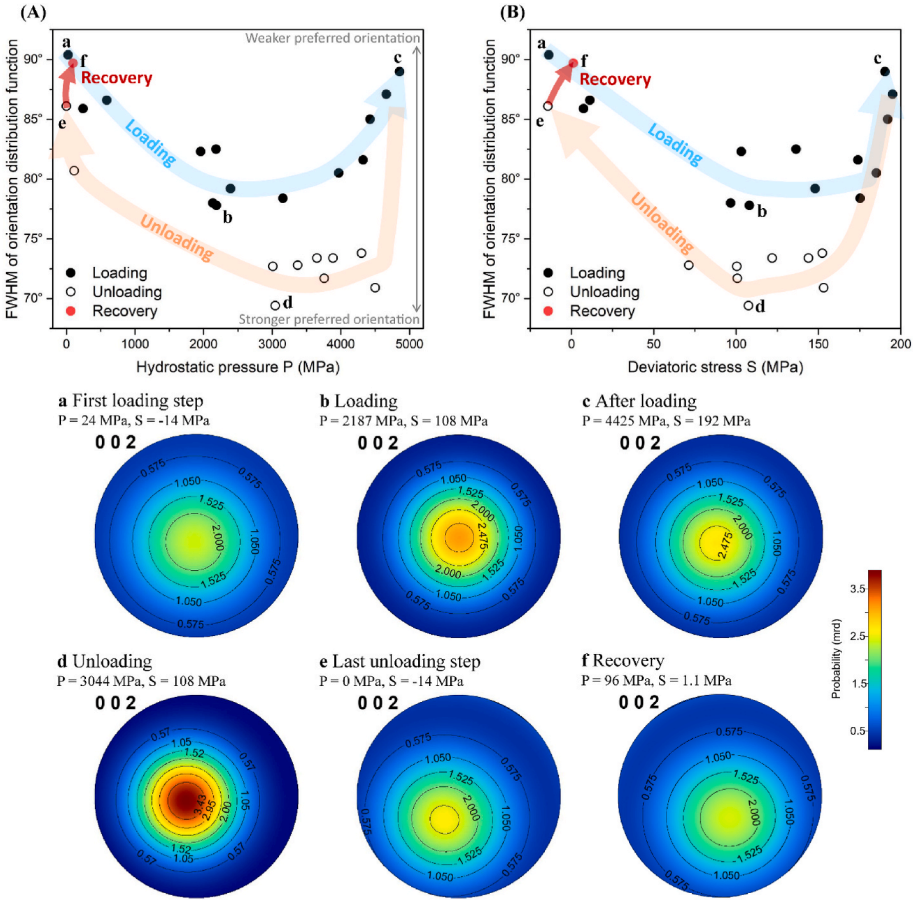

Fig. 7. (A) FWHM of the orientation distribution function as a function of the hydrostatic pressure P and (B) FWHM of the orientation distribution function as a function of the deviatoric stress S. The pole figures of C–S–H (002) plane corresponding to the representative data points a-f labeled in (A) and (B) are presented. The contours in the pole figures display the texture intensity in the unit of m.r.d.

comparable stress state. It was only after the 6-hr recovery (step f) that the recovered texture resumed to the level at the first loading step, evidenced by the comparable probability distribution of the C–S–H (002) plane in the unit of m.r.d. shown in the pole figures Fig. 7a and f. This observation suggests the time-dependent nature of the evolution of the C–S–H preferred orientation and that nonnegligible permanent preferred orientation could exist well after the removal of applied stresses. The findings may shed light on the creep and relaxation mechanisms of cement-based and alkali-activated materials.

The different types of changes to the C–S–H nanocrystallites under different stress levels resulted in the intensifying and weakening of the C–S–H preferred orientation (Fig. 8). On the loading path before reaching S ~0.1 GPa, a stronger texture formed with the consolidation of the C–S–H nanocrystallites in the compressed chamber. Intergranular pores were removed through the increasing alignment of C–S–H nanocrystallites – their *c*-axis (the softest axis) preferentially oriented toward the compressive deviatoric stress (Fig. 8, left to the middle) and through the pressure-induced closer contact of C–S–H nanocrystallites [20]. The incompressibility of the *c*-axis is always the lowest in C–S–H, C-A-S-H, and tobermorite [11,34,40]. Thus, the first few loading steps in this study represent this scenario. Similar observations have been found in our previous study: the softest axis of the (nano)crystals, e.g., cross-linked C-A-S-H (the *c*-axis), portlandite (the *c*-axis), and ettringite (the *a*-axis), is subject to preferential re-orientation towards the compression direction [41].

The following plateau and drop in texture intensity upon further loading at S > 100 MPa were attributed to the impact of internal transformations of C–S–H nanocrystallites. This transformation within C–S–H nanocrystallites counterbalances or even diminishes the efficacy of *c*-axis alignment on texture development. The crystal length along the *c*-axis was consistently refined to ~5 nm at all stress levels, and the *c*-axis length of C–S–H unit cells constantly maintained a negative linear correlation with the pressure. This fact suggests no splitting between the layers, namely a constant number of layers of C–S–H nanocrystallites. Accordingly, we propose two types of change in C–S–H nanocrystallites to account for the observed weakening texture – greater FWHM, or equivalently, lower maximum m.r.d. – during the latter half of the loading (Fig. 8, middle to the right):

First, compressive stress-induced interlayer sliding above 100 MPa could result in weakened (002) diffraction (Fig. 8, top right). A similar sliding in layer structures has been found in mica at shear stress at hundreds of MPa [42]. Therefore, the interlayer sliding would be most predominant in C–S–H nanocrystallites whose *c*-axis closely oriented to the compressive deviatoric stress. Meanwhile, for those less aligned nanocrystallites experiencing lower compressive stress, the (002) diffraction was less affected due to less interlayer sliding. As a result, the (002) diffraction of nanocrystallites most preferentially oriented toward the loading direction (i.e., contributing to the maximum m.r.d. in the pole figures) was weakened most significantly. This differential interlayer sliding thus caused a reduction in refined texture intensity at higher stress levels. A similar layer sliding behavior is also found in a high-pressure study of non-cross-linked C–S–H using XRD and small angle scattering [43].

Second, compressive stress-induced breakage of the nanocrystallites across the silicate chain could also explain the observed texture evolution near the end of the loading path (Fig. 8, bottom right). It has been evidenced in non-cross-linked C–S–H (Ca/Si = 1) that the ratio between Q^1 and Q^2 silicate increased at deviatoric stress ~200 MPa, suggesting breakage of silicate chains [44]. The condition agrees with the present scenario where the weakening of the texture happened at S ~100 MPa. In contrast to the Q^2-containing C–S–H in the previous study, the present C–S–H at Ca/Si ~1.5 is dominated by Q^1 silicate dimers and vacant bridging sites [32]. As the Ca–O ionic bonding or a vacant bonding site is weaker than Si–O covalent bonding, the breakage across the silicate chains could be initiated at lower deviatoric stress levels in the present sample. Our recent high-pressure X-ray Raman scattering study also suggested the sliding at C–S–H interlayers at Ca/Si = 1.3 under hundreds of MPa of deviatoric stress [45].

The weakening of the texture upon loading is not observed in our previous HP-XRD study of cross-linked C-A-S-H [17]. This differential behavior between cross-linked C-A-S-H and the present non-cross-linked C–S–H is reasonable because the C-A-S-H was cross-linked with considerably longer chains compared to the present C–S–H. The strong Si–O–Al covalent bonding in C-A-S-H could prohibit either interlayer sliding or breakage across aluminosilicate chains. This mechanical behavior of cross-linking sites is consistent with a recent molecular dynamics simulation of crystalline C-A-S-H [46].

The significant rise and fall in texture intensity during unloading could be accounted for by the competition between decreasing deviatoric stress (hindering texture formation) and increasing nanogranular mobility (facilitating texture formation). At the beginning of unloading, the latter was more effective: the free space suddenly released from unscrewing the DAC would perturb C–S–H nanocrystallites; reduced intergranular friction eases further texture development where the relative motion between nanocrystallites might have been suppressed before unloading due to steric obstructions. By the end of unloading, the tilt of the texture fiber component from the *Z*-axis suggested that the recovered chamber had limited confinement to the compacted C–S–H. This tilt is also found in a previous HP-XRD study of cross-linked C-A-S-H during the unloading of deviatoric stress [17]. The C–S–H compact experienced a permanent partial removal of intergranular pores. This significant pressure-induced porosity change of C–S–H compacts is supported by a recent study [20], where the gel porosity is lowered by 20–40% under 2000 MPa compaction. Therefore, the low deviatoric stress level in the present study dominated the obvious weakening of the preferred orientation, while the high intergranular mobility was

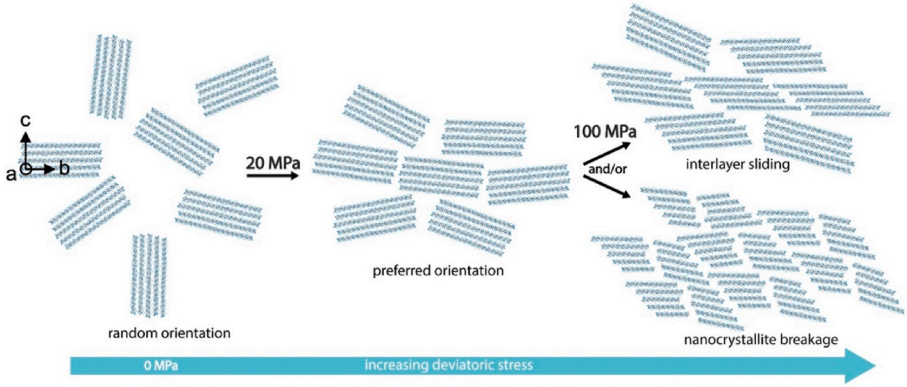

Fig. 8. Schematic representation of the change to non-cross-linked C–S–H nanocrystallites under an increasing deviatoric stress. Green/brown straight strokes represent the basal layers of C–S–H. (For interpretation of the references to colour in this figure legend, the reader is referred to the Web version of this article.)

scarcely beneficial in the absence of substantial deviatoric stress, the real driving force of C–S–H texture formation.

Our recent study unveiled the time-dependent and water-facilitated development of the preferred orientation of C-A-S-H nanocrystallites under a sustained load [41]. This nanocrystal preferred orientation has been correlated to the time-dependent creep of concrete. The noticeable weakening and retaining of the preferred orientation through the 6-hr recovery in the present study have refined the correlation between C–S–H preferred orientation development and creep and relaxation behaviors of concrete. This improvement in understanding C–S–H preferred orientation is achieved in a more practical level of deviatoric stress in the present study. There have been intense debates on the origin of C–S–H creep. One viewpoint emphasizes the role of interlayer water [47] which, more specifically, contributes to the creep of C–S–H through the facilitation of stress-induced interlayer translation [27]. On the other side, Thomas and Jennings [48] proposed the creep of cement pastes to the re-organization of C–S–H nanoglobules under stress, and Haist et al. [49] ascribed the C–S–H creep to slippage between the nanoglobules. A recent micro-indentation study [50] indicated that adsorbed water in hardened pastes facilitates the sliding between C–S–H nanoglobules. The critical water content for sliding free energy barrier of C–S–H was simulated in Ref. [51]. The present study provides direct evidence favorable to the intergranular re-organization standpoint and supplements by specifying the nanogranular re-arrangement pattern: at deviatoric stresses of 10s of MPa, the typical stress level of cement-based and alkali-activated materials under service [52,53], creep occurs as a result of the preferential re-orientation of the C–S–H nanocrystallites *c*-axis to the compressive deviatoric stress. Note that hydrostatic pressure does not induce any change in crystal orientation. Although interlayer sliding has been proposed as the creep mechanism of cement-based materials, e.g., concrete [27], the required deviatoric stress for interlayer sliding is much higher than the stress level of concrete under service. It is only at elevated deviatoric stresses (>∼100 MPa) that the intra-particle transformations (e.g., interlayer sliding) occur, which thus is not the origin of creep of concrete under service-condition. Note that we do not eliminate the contribution of cement hydration on creep mechanisms [54,55] as hydration increases packing density and reduces the distance between outer product C–S-Hs, thus increasing the intergranular barrier for C–S–H preferred orientation.

As mentioned above, the deformation of the C–S–H nanocrystallite itself, e.g., interlayer sliding, seems to be unlikely to happen in real concrete structures in service life, but that may unavoidably occur in nanoindentation experiments where the local deviatoric stress could readily exceed 100s MPa [13,56], typically from 500 MPa to 2 GPa. As a result, the properties (e.g., Young's modulus and creep modulus) of the cement-based materials characterized by nanoindentation may differ from the properties of the same materials under service conditions. The elastic modulus and creep modulus of C–S–H fitted from their microchemical properties in nanoindentation studies cannot correctly reflect the influences of high deviatoric stress on the C–S–H nanocrystallite orientation. For example in a recent study [57], besides the high degree of carbonation of C–S–H, the influences of compaction load levels on the development of preferred orientation were also ignored, which are critical [41,58]. Nevertheless, micro-indentation, where the applied deviatoric stress could be controlled well below 100 MPa, could be an asset to examining the mechanical properties and creep behavior of cement-based materials so as to advance the understanding of the mechanical behaviors of concrete and to provide reliable inputs for multi-scale simulations of concrete under practical service conditions. Our findings provide new knowledge to computational studies (e.g., molecular dynamics) where the preferred orientation of C–S–H nanocrystallites (also known as building blocks) is largely neglected for decades.

The behaviors of C–S–H have both instantaneous responses (elastic and plastic) and time-dependent responses. An elastic response is always present through the constitutive relation based on the stiffness tensor of each phase, while a plastic response could result from the proposed interlayer sliding and/or nanocrystallite breakage mechanism. Due to the presence and mobility of water in interlayers and between nanocrystallites (i.e., interlayer water and gel water) [20,41,43] of C–S–H, we also expect additional time-dependent behaviors following viscoelasticity, in analogue to the relaxation and creep in typical cement-based systems.

For future studies, the HP-XRD experiments may be improved to benefit further research with new knowledge. The time of sustained stress and stress recovery may be extended to tens/hundreds of days in future experiments to further the understanding of the time-dependent behavior of C–S–H if the precious beamtime is available and the use of a DAC is well-managed. The control of stress levels is challenging since no pressure-transmitting medium can be used for deviatoric stress conditions and the deformations of the gasket and C–S–H are inelastic. The stress level could be lowered if a larger pair of diamond is used. The diamond culet diameter in this study is ∼400 μm. The maximum culet diameter of the diamond used for HP-XRD is typically ∼1 mm.

4. Conclusions

The development of the preferred orientation of C–S–H nanocrystallites under compressive loading was studied with high-pressure XRD using DAC in radial geometry. The preferred orientation of C–S–H nanocrystallites clearly occurs at deviatoric stress as low as ∼12 MPa. The texture is developed through the preferential re-orientation of the C–S–H nanocrystallites *c*-axis (normal to the basal plane) towards the direction of compressive deviatoric stress at < ∼100 MPa. Above 100 MPa, texture creases growing and followed by texture weakening, suggesting a transition of C–S–H behavior under deviatoric stress – from intergranular re-organization to transformations within C–S–H nanocrystallite. The creep mechanism of concrete, under tens of MPa compression, is the preferential alignment of C–S–H nanocrystallites *c*-axis to the compressive stress, accompanied by removal of intergranular pores. Interlayer translation within C–S–H nanocrystallites, which occurs at deviatoric stress over 100 MPa, is not the mechanism of concrete under service as this stress level is above the typical service loads of concrete. Experimental characterization of mechanical properties and creep of cement-based and alkali-activated materials should be designed with care. Tools that provide high deviatoric stress, e.g., nanoindentation, should be carefully used in the evaluation and modeling of cement-based materials, with the consideration of C–S–H nanocrystallites preferred orientation and translation within C–S–H nanocrystallite itself. Experimental techniques capable of providing deviatoric stress under tens of MPa and precluding transformation within C–S–H nanocrystallite are suggested for the study of concrete mechanical behaviors. Computational studies should consider C–S–H preferred orientation under even just tens of MPa deviatoric stress and translation within C–S–H nanocrystallites (e.g., interlayer sliding and breakage of silicate chains) at over 100 MPa into their models.

Author statement

Jiaqi Li: Conceptualization, Methodology, Formal analysis, Investigation, Validation, Visualization, Writing - Original Draft, Supervision, Funding acquisition; Wenxin Zhang: Formal analysis, Visualization, Writing - Review & Editing.

Declaration of competing interest

The authors declare that they have no known competing financial interests or personal relationships that could have appeared to influence the work reported in this paper.

Data availability

Data will be made available on request.

Acknowledgement

This work was performed under the auspices of the U.S. Department of Energy by Lawrence Livermore National Laboratory (contract No. DE-AC52-07NA27344). Beamline 12.2.2 and the sample preparation of this research are partially supported by COMPRES, the Consortium for Materials Properties Research in Earth Sciences under NSF Cooperative Agreement EAR 1606856. This work is supported by the US National Science Foundation under Division of Materials Research Ceramics Program, DMR-CER, Grant No. 1935604. We appreciate Dr. Martin Kunz and Dr. Jinyuan Yan at ALS for beamtime support. The Advanced Light Source is supported by the Director, Office of Science, Office of Basic Energy Sciences, of the U.S. Department of Energy under Contract No. DE-AC02-05CH11231. LLNL IM number: LLNL-JRNL-832129.

References

[1] Mehta PK, Monteiro PJ. Concrete microstructure, properties and materials. New York: McGraw-Hill; 2017.
[2] Chen B, Qiao G, Hou D, Wang M, Li Z. Cement-based material modified by in-situ polymerization: from experiments to molecular dynamics investigation. Compos B Eng 2020;194:108036.
[3] Chi Y, Huang B, Saafi M, Ye J, Lambert C. Carrot-based covalently bonded saccharides as a new 2D material for healing defective calcium-silicate-hydrate in cement: integrating atomistic computational simulation with experimental studies. Compos B Eng 2020;199:108235.
[4] Skinner LB, Chae SR, Benmore CJ, Wenk HR, Monteiro PJM. Nanostructure of calcium silicate hydrates in cements. Phys Rev Lett 2010;104:195502.
[5] Kang X, Zhu X, Liu J, Shu X, Huang Y, Qian J. Dissolution and precipitation behaviours of graphene oxide/tricalcium silicate composites. Compos B Eng 2020;186:107800.
[6] Richardson IG, Groves GW. Microstructure and microanalysis of hardened ordinary portland-cement pastes. J Mater Sci 1993;28:265–77.
[7] Richardson IG. The calcium silicate hydrates. Cement Concr Res 2008;38:137–58.
[8] John E, Matschei T, Stephan D. Nucleation seeding with calcium silicate hydrate - a review. Cement Concr Res 2018;113:74–85.
[9] Bonaccorsi E, Merlino S, Kampf AR. The crystal structure of tobermorite 14 A (Plombierite), a C-S-H phase. J Am Ceram Soc 2005;88:505–12.
[10] Cong XD, Kirkpatrick RJ. Si-29 MAS NMR study of the structure of calcium silicate hydrate. Adv Cement Base Mater 1996;3:144–56.
[11] Geng G, Myers RJ, Qomi MJA, Monteiro PJM. Densification of the interlayer spacing governs the nanomechanical properties of calcium-silicate-hydrate. Sci Rep 2017;7:10986.
[12] Gardner DW, Li J, Morshedifard A, Masoumi S, Abdolhosseini Qomi MJ, Monteiro PJ, et al. Silicate bond characteristics in calcium-silicate-hydrates determined by high pressure Raman spectroscopy. J Phys Chem C 2020;124(33):18335–45.
[13] Vandamme M, Ulm F-J. Nanogranular origin of concrete creep. Proc Natl Acad Sci USA 2009;106:10552–7.
[14] Pichler B, Hellmich C, Eberhardsteiner J, Wasserbauer J, Termkhajornkit P, Barbarulo R, Chanvillard G. Effect of gel-space ratio and microstructure on strength of hydrating cementitious materials: an engineering micromechanics approach. Cement Concr Res 2013;45:55–68.
[15] Nguyen-Sy T, Nguyen T-K, Dao V-D, Le-Nguyen K, Vu N-M, To Q-D, Nguyen T-D, Nguyen T-T. A flexible homogenization method for the effective elastic properties of cement pastes with w/c effect. Cement Concr Res 2020;134:106106.
[16] Hu ZL, Wyrzykowski M, Griffa M, Scrivener K, Lura P. Young's modulus and creep of calcium-silicate-hydrate compacts measured by microindentation. Cement Concr Res 2020;134.
[17] Geng G, Vasin RN, Li J, Qomi MJA, Yan J, Wenk HR, Monteiro PJM. Preferred orientation of calcium aluminosilicate hydrate induced by confined compression. Cement Concr Res 2018;113:186–96.
[18] Wenk HR. Preferred orientation in deformed metal and rocks: an introduction to modern texture analysis. Elsevier 2016.
[19] Ruan S, Yang E, Unluer C. Production of reactive magnesia from desalination reject brine and its use as a binder. J. CO2 Util. 2021;44:101383.
[20] Zhang Z, Yan Y, Qu Z, Geng G. Endowing strength to calcium silicate hydrate (CSH) powder by high pressure mechanical compaction. Cement Concr Res 2022;159:106858.
[21] Wenk H-R, Monteiro PJ, Kunz M, Chen K, Tamura N, Lutterotti L, Del Arroz J. Preferred orientation of ettringite in concrete fractures. J Appl Crystallogr 2009;42:429–32.
[22] Zhu L, Wang J-J, Li X, Zhao G-Y, Huo X-J. Experimental and numerical study on creep and shrinkage effects of ultra high-performance concrete beam. Compos B Eng 2020;184:107713.
[23] Bazant ZP, Chern J. Concrete creep at variable humidity: constitutive law and mechanism. Mater Struct 1985;18:1.
[24] Rossi P, Tailhan JL, Le Maou F. Comparison of concrete creep in tension and in compression: influence of concrete age at loading and drying conditions. Cement Concr Res 2013;51:78–84.
[25] Jennings HM. Colloid model of C– S– H and implications to the problem of creep and shrinkage. Mater Struct 2004;37:59–70.
[26] Bazant ZP, Hauggaard AB, Baweja S, Ulm FJ. Microprestress-solidification theory for concrete creep .1. Aging and drying effects. J Eng Mech-Asce 1997;123:1188–94.
[27] Alizadeh R, Beaudoin JJ, Raki L. Viscoelastic nature of calcium silicate hydrate. Cement Concr Compos 2010;32:369–76.
[28] Li XD, Grasley ZC, Bullard JW, Feng P. Creep and relaxation of cement paste caused by stress-induced dissolution of hydrated solid components. J Am Ceram Soc 2018;101:4237–55.
[29] Wang Y, Cao Y, Zhang Z, Huang J, Zhang P, Ma Y, Wang H. Study of acidic degradation of alkali-activated materials using synthetic C-(N)-ASH and NASH gels. Compos B Eng 2022;230:109510.
[30] Cao R, Zhang S, Banthia N, Zhang Y, Zhang Z. Interpreting the early-age reaction process of alkali-activated slag by using combined embedded ultrasonic measurement, thermal analysis, XRD, FTIR and SEM. Compos B Eng 2020;186:107840.
[31] Li C. Degradation mechanism of blended cement pastes in sulfate-bearing environments under applied electric fields: sulfate attack vs. decalcification, Composites Part B: Engineering. 2022.
[32] L'Hôpital E, Lothenbach B, Kulik D, Scrivener K. Influence of calcium to silica ratio on aluminium uptake in calcium silicate hydrate. Cement Concr Res 2016;85:111–21.
[33] Kantor I, Prakapenka V, Kantor A, Dera P, Kurnosov A, Sinogeikin S, Dubrovinskaia N, Dubrovinsky L. BX90: a new diamond anvil cell design for X-ray diffraction and optical measurements. Rev Sci Instrum 2012;83:125102.
[34] Li J, Zhang W, Monteiro PJM. The structure and intrinsic mechanical properties of nanocrystalline calcium silicate hydrate. ACS Sustainable Chem Eng 2020;8:12453–61.
[35] Li J, Zhang W, Monteiro PJ. Mechanical properties of struvite-K: a high-pressure X-ray diffraction study. Cement Concr Res 2020;136:106171.
[36] Singh AK. The lattice strains in a specimen (cubic system) compressed nonhydrostatically in an opposed anvil device. J Appl Phys 1993;73:4278–86.
[37] Wenk H-R, Lutterotti L, Kaercher P, Kanitpanyacharoen W, Miyagi L, Vasin R. Rietveld texture analysis from synchrotron diffraction images. II. Complex multiphase materials and diamond anvil cell experiments. Powder Diffr 2014;29:220–32.
[38] Matthies S, Priesmeyer HG, Daymond MR. On the diffractive determination of single-crystal elastic constants using polycrystalline samples. J Appl Crystallogr 2001;34:585–601.
[39] Lutterotti L, Vasin R, Wenk H-R. Rietveld texture analysis from synchrotron diffraction images. I. Calibration and basic analysis. Powder Diffr 2014;29:76–84.
[40] Li J, Zhang W, Garbev K, Beuchle G, Monteiro PJ. Influences of cross-linking and Al incorporation on the intrinsic mechanical properties of tobermorite. Cement Concr Res 2020;136:106170.
[41] Li J, Zhang W, Monteiro PJ. Preferred orientation of calcium aluminosilicate hydrate compacts: implications for creep and indentation. Cement Concr Res 2021;143:106371.
[42] Mares VM, Kronenberg AK. Experimental deformation of muscovite. J Struct Geol 1993;15:1061–75.
[43] D.W. Gardner, J. Li, et al, Uniaxial stress increases layer stacking disorder in calcium silicate hydrates, Acta Mater, (Under Review).
[44] Gardner DW, Li J, Kunz M, Zhu C, Monteiro PJ, Maboudian R, Carraro C. Plastic deformation mechanism of calcium-silicate hydrates determined by deviatoric-stress Raman spectroscopy. Cement Concr Res 2021;146:106476.
[45] Li J, Zhang W, Monteiro PJ. Synchrotron X-ray Raman scattering shows the changes of the Ca environment in CSH exposed to high pressure. Cement Concr Res 2020;132:106066.
[46] Dupuis R, Moon J, Jeong Y, Taylor R, Kang S-H, Manzano H, Ayuela A, Monteiro PJ, Dolado JS. Normal and anomalous self-healing mechanism of crystalline calcium silicate hydrates. Cement Concr Res 2021;142:106356.
[47] Feldman RF. Mechanism of creep of hydrated Portland cement paste. Cement Concr Res 1972;2:521–40.
[48] Thomas JJ, Jennings HM. A colloidal interpretation of chemical aging of the C-S-H gel and its effects on the properties of cement paste. Cement Concr Res 2006;36:30–8.
[49] Haist M, Divoux T, Krakowiak KJ, Skibsted J, Pellenq RJ-M, Müller HS, Ulm F-J. Creep in reactive colloidal gels: a nanomechanical study of cement hydrates. 2020. arXiv preprint arXiv:2008.02617.
[50] Suwanmaneechot P, Aili A, Maruyama I. Creep behavior of CSH under different drying relative humidities: interpretation of microindentation tests and sorption measurements by multi-scale analysis. Cement Concr Res 2020;132:106036.
[51] Masoumi S, Valipour H, Abdolhosseini Qomi MJ. Interparticle interactions in colloidal systems: toward a comprehensive mesoscale model. ACS Appl Mater Interfaces 2017;9:27338–49.
[52] Ke X, Duan Y. Coupling machine learning with thermodynamic modelling to develop a composition-property model for alkali-activated materials. Compos B Eng 2021;216:108801.
[53] Panda B, Ruan S, Unluer C, Tan MJ. Investigation of the properties of alkali-activated slag mixes involving the use of nanoclay and nucleation seeds for 3D printing. Compos B Eng 2020;186:107826.

[54] Wyrzykowski M, Scrivener K, Lura P. Basic creep of cement paste at early age - the role of cement hydration. Cement Concr Res 2019;116:191–201.
[55] Lavergne F, Barthélémy J-F. Confronting a refined multiscale estimate for the aging basic creep of concrete with a comprehensive experimental database. Cement Concr Res 2020;136:106163.
[56] Wilson W, Sorelli L, Tagnit-Hamou A. Automated coupling of Nanolndentation and Quantitative Energy-Dispersive Spectroscopy (NI-QEDS): a comprehensive method to disclose the micro-chemo-mechanical properties of cement pastes. Cement Concr Res 2018;103:49–65.
[57] Wang J, Hu Z, Chen Y, Huang J, Ma Y, Zhu W, Liu J. Effect of Ca/Si and Al/Si on micromechanical properties of C (-A)-SH. Cement Concr Res 2022;157:106811.
[58] Hay R, Li J, Celik K. Influencing factors on micromechanical properties of calcium (alumino) silicate hydrate C-(A-) SH under nanoindentation experiment. Cement Concr Res 2020;134:106088.